THE JOURNAL OF PHYSICAL CHEMISTRY C

pubs.acs.org/JPCC Article

Morphology Evolution of FCC and HCP Cobalt Induced by a CO Atmosphere from *Ab Initio* Thermodynamics

Hao Lin, Jin-Xun Liu, Hong-Jun Fan,* and Wei-Xue Li*

Cite This: https://dx.doi.org/10.1021/acs.jpcc.0c07386 Read Online

ABSTRACT: Fischer–Tropsch synthesis, the conversion of CO and H_2 to long-chain hydrocarbons, is performed at relatively low temperatures and high pressures over the most commonly encountered iron-, ruthenium-, or cobalt-based catalysts. Identification of the morphologies and structure evolution of FTS catalysts under reaction conditions are essential for understanding the structure–reactivity relationship. In this work, we performed a comprehensive *ab initio* thermodynamics study to provide an understanding of the morphology evolution of cobalt (Co) catalyst with hexagonal close-packed (HCP) and face-centered cubic (FCC) crystal structures under a CO atmosphere. CO adsorption on numerous surfaces of HCP Co and FCC Co at different coverages were investigated. On both HCP Co and FCC Co, lateral interaction is attractive at lower coverage and becomes repulsive at higher coverage. Compared to FCC Co, though in average CO adsorption on HCP Co is stronger at lower coverage, they become similar at higher coverage due to the overwhelming lateral repulsion. We established the phase diagrams and the morphology evolution of FCC Co and HCP Co as a function of CO chemical potentials. The most probable exposed facets in FCC Co and HCP Co Wulff shapes were revealed under different CO atmospheres. At a relatively low CO chemical potential, many open facets could be exposed in Co equilibrium morphology, including $\{10\bar{1}2\}$, $\{10\bar{1}1\}$, $\{10\bar{1}0\}$, and $\{11\bar{2}0\}$ facets for HCP Co and {311}, {110}, and {100} facets for FCC Co. In contrast, at a relatively high CO chemical potential, FCC Co has an octahedron shape composed entirely by close-packed {111} facets, while HCP Co is hexagonal prism shaped composed mainly by close-packed {0001} and $\{10\bar{1}0\}$ facets. The morphology evolution of HCP and FCC phases would have great impact on the inherited catalytic performance of Co nanoparticles, thus will selectively regulate their chemical reactivity.

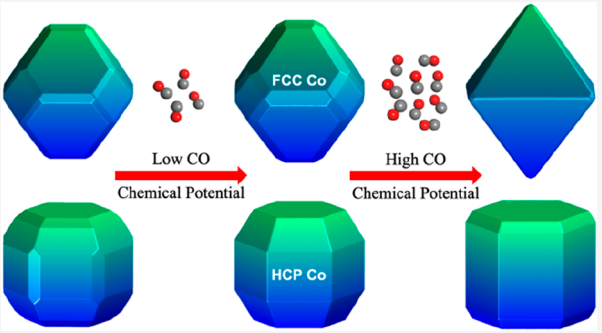

INTRODUCTION

Metal nanoparticles (NPs) have attracted intensive attention for their wide applications as heterogeneous catalysts in chemicals, optical, automobile, and petroleum industries.[1−4] In principle, the catalytic performance of metal NPs is mainly determined by their sizes and shapes.[5−7] *In situ* characterizations showed that metal NPs may undergo reshaping, surface reconstruction, and phase transformation dynamically and usually reversibly under reaction conditions,[8−12] which has a great influence on the performance of the catalysts in turn.[13] Therefore, identification of the morphology and surface structures of metal NPs catalysts, especially in *operando* reaction conditions, is still an important yet challenging issue in heterogeneous catalysis.[14,15]

Fischer–Tropsch synthesis (FTS) is a series of chemical reactions that convert CO and H_2 from coal, natural gas, and biomass to liquid fuels and valuable chemicals at a high pressure of about 20 bar and typical rather low temperature between 190 and 260 °C, in reality at a high CO coverage.[16−18] The most commonly encountered active catalysts for FTS are based on iron (Fe), ruthenium (Ru), and cobalt (Co) metals.[19−21] Among them, Co is considered to be a good choice for FTS attributed to its moderate price and high activity/selectivity for generating long-chain hydrocarbons at mild temperatures.[22,23] The Co-catalyzed FTS reaction has typically been recognized as a complex structure-sensitive reaction, which is controlled by the crystal size of the catalyst.[24,25] A number of works indicated that there was a gradual decrease in the turnover frequency when Co particles size are smaller than 6 nm.[26−29] The origin of the Co particle size effect on FTS is still in a great debate due to the complexity of the FTS and lack of structural information about the catalyst under *operando* FTS reaction conditions. Overwhelming evidence indicates that Co would transform from hexagonal close-packed (HCP) phase to face-centered cubic (FCC) one when the particle size scales down to several

Received: August 12, 2020
Revised: September 22, 2020
Published: September 28, 2020

nanometers.[30,31] Because FCC Co with a higher bulk energy has a lower surface energy as compensation than HCP Co, which provides a driving force for the size-induced HCP → FCC phase transition of Co nanoparticles.[32] A deep understanding of the crystal phase effect of Co-based catalysts on FTS is therefore essential for guiding better catalyst design.

The crystal phase effect has gained considerable interest in heterogeneous catalysis nowadays.[33−35] The great impact of crystal phases on catalysis is often considered to be originated from their distinct bulk symmetries, resulting in different morphologies and various structural motifs with totally different reactivity.[36,37] Multiple experimental groups concluded that HCP Co has higher FTS activity than FCC Co, which is probably originated from a higher density of surface defects and stacking faults in HCP Co.[38,39] On the basis of first-principles kinetic modeling, we discovered that HCP Co displays higher activity for CO activation than FCC Co, mainly came from the exposure of more open surfaces with higher intrinsic activities in HCP Co.[40] Our theoretical finding is corroborated by recent experimental measurement that HCP Co is more active than FCC Co for CO activation, and HCP Co presents a lower activation energy for FTS than FCC Co by 0.43 eV.[41] Besides the activity, the selectivity of FTS is strongly dependent on the crystal phase of Co as well. By density functional theory (DFT) calculations, Zhang et al. revealed that HCP Co is more selective to chain growth than FCC Co because of the different carbon chain growth mechanism underlying these two different Co phases.[42] This theoretical finding is in line with the experimental measurement that HCP Co displays less methane selectivity than FCC Co.[43] Although previous DFT calculations were all performed at a low CO coverage, a qualitative agreement between experimental observations and DFT calculations was demonstrated. However, Co nanoparticles would be covered by CO with high coverages under typical FTS conditions, which may have a great influence on the morphologies of HCP Co and FCC Co. Because FTS activity and selectivity are sensitive to the morphology and crystal phase of Co, it is thus desirable to identify the morphology evolution of HCP Co and FCC Co under a CO atmosphere.

In this work, we performed a comprehensive DFT calculation to understand the morphologies evolution of HCP Co and FCC Co under a wide range of CO chemical potentials. The CO adsorption dependence on the crystal structures of Co at different CO coverages was first studied. Then, the thermodynamic equilibrium morphologies of HCP Co and FCC Co were obtained via the Wulff construction based on the calculated surface free energies, which are CO chemical potential dependent. The most probable exposed facets, which should be considered in the future work of HCP Co and FCC Co, were revealed under different CO atmospheres. The influence of CO adsorption on HCP → FCC phase transition is finally discussed. The different morphological evolution between HCP and FCC phases under CO atmosphere may have a consequential impact on the inherited catalytic performance of Co nanoparticles, which could be helpful to improve the FTS catalyst design.

COMPUTATIONAL DETAILS

Methods. All the spin-polarized DFT calculations for CO adsorption on different facets of HCP Co and FCC Co were performed by using the Vienna *Ab initio* Simulation Package (VASP)[44−46] within the projector augmented wave (PAW) approach.[47,48] The Perdew−Burke−Ernzerhof (PBE) generalized gradient approximation (GGA) exchange-correlation functional was employed,[49,50] and the plane wave cutoff energy was specified by 400 eV. The energy and maximum force convergence thresholds were specified by 10^{-5} eV and 0.01 eV/Å, respectively. The Methfessel−Paxton method was chosen as the smearing algorithm,[51] and the blocked Davidson iteration scheme was applied as the electron minimization algorithm.[52] We used a vacuum thickness of 15 Å to avoid the interactions between neighboring slabs to ensure convergence. We took the FCC Co (111) surface as an example below to describe the computational details. The Co (111) surface was modeled with a five-layer slab. Hundreds of CO adsorption configurations at a specific coverage were sampled. Particularly, we adopted $p(2 \times 2)$, $p(3 \times 3)$, $c(4 \times 2)$, $(2\sqrt{3} \times 2\sqrt{3})R30°$, $c(\sqrt{3} \times 5)$rect, and $c(\sqrt{3} \times 3)$rect slabs to study CO coverage effect with CO coverages varying continuously from low to high. Correspondingly, Monkhorst−Pack[53] grids of $(5 \times 5 \times 1)$, $(3 \times 3 \times 1)$, $(2 \times 4 \times 1)$, $(3 \times 3 \times 1)$, $(5 \times 2 \times 1)$, and $(5 \times 3 \times 1)$ were used to ensure k-point sampling convergence, respectively. The bottom two layers were constrained at their bulk positions, and the top three Co layers and adsorbed CO molecules were allowed to relax. All the other HCP Co and FCC Co surfaces were simulated by four or five equivalent (111) layers with the k-point density kept at ∼0.05/Å.

For a given surface, the average CO adsorption energy is calculated by

$$E_{ad}(\theta_C) = (E_{CO/slab} - E_{slab} - N \times E_{CO})/N \quad (1)$$

where $E_{CO/slab}$, E_{slab}, and E_{CO} are the total energies of Co surface with adsorbed CO, clean Co surface, and gaseous CO molecule, respectively. N is the number of adsorbed CO molecules, and θ_C is the conventional CO fractional coverage. Herein, CO coverage of one monolayer (ML) corresponds to one CO molecule adsorbing at each primitive cell of the Co surface.

Thermodynamic Phase Diagram. *Ab initio* atomistic thermodynamics analysis[54−56] is a useful tool to identify the most stable CO adsorption configurations at different CO chemical potentials over HCP Co and FCC Co facets. For a given surface, the surface free energy at temperature T and partial pressure p can be calculated by the summation of clean surface energy γ_{clean} and CO adsorption free energy $\Delta\gamma_{CO}(T,p)$:[57,58]

$$\gamma(T, p) = \gamma_{clean} + \Delta\gamma_{CO}(T, p) \quad (2)$$

where

$$\Delta\gamma_{CO}(T, p) = N[E_{ad}(\theta) - \Delta\mu_{CO}(T, p)]/A_S \quad (3)$$

where $\Delta\mu_{CO}(T,p) = \mu_{CO}(T,p_0) + k_BT \ln(p/p_0)$, $\mu_{CO}(T,p_0)$ is the chemical potential of CO at temperature T (p_0 = 1 bar), and A_S is the surface area of the Co surface.

By using the calculated surface free energies, we can obtain the equilibrium morphology of a freestanding particle by the Gibbs−Wulff theorem.[59] The Wulff construction can be executed as follow: starting from a center point, a plane that is normal to the ⟨hkl⟩ vector (taking FCC Co as an example) is drawn at a distance of $d_{hkl} = C \times \gamma_{hkl}$, where C is a constant value and γ_{hkl} is the surface energy. Once this process is repeated for all the Miller-index planes, the polyhedron that lines inside all the planes gives the equilibrium morphology of the crystal. Our previous theoretical work demonstrates that

https://dx.doi.org/10.1021/acs.jpcc.0c07386
J. Phys. Chem. C XXXX, XXX, XXX−XXX

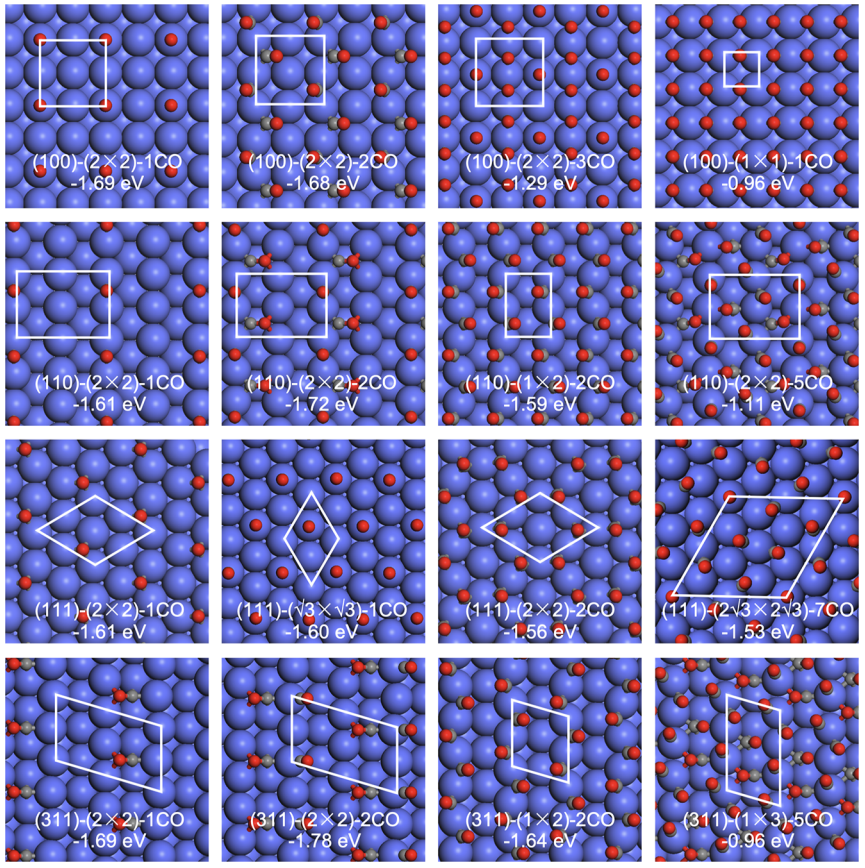

Figure 1. Optimized CO adsorption configurations and corresponding average adsorption energies (eV) at different coverages over FCC Co facets.

under vacuum conditions there are generally four groups of facets exposed in FCC Co Wulff shape, namely, {111}, {100}, {110}, and {311}, and five group of facets exposed in HCP Co Wulff shape, namely, {0001}, $\{10\bar{1}1\}$, $\{10\bar{1}0\}$, $\{10\bar{1}2\}$, and $\{11\bar{2}0\}$.[40] We used these indicated nine facets as a starting point to investigate CO coverage effect on the morphology evolution between HCP Co and FCC Co, and more facets may be considered in our future work. The Wulff shapes of HCP Co and FCC Co in the present work were visualized by VESTA software.[60]

RESULTS AND DISCUSSION

CO Adsorption Structures and Average Adsorption Energies. The structure sensitivity of CO adsorption was first studied over the four and five facets stated above in FCC Co and HCP Co Wulff shapes, respectively. Many types of adsorption sites, including top, bridge, 3-fold, and 4-fold hollow sites, as well as other sites (such as B_5) were considered in the present work to evaluate CO coverage effect on different HCP and FCC Co facets. The most stable CO adsorption configurations and corresponding average CO adsorption energies at different coverages over FCC Co and HCP Co facets are summarized in Figures 1 and 2 as well as Figures S1 and S2.

The most favorable CO adsorption site is closely related to the surface orientations and topologies of FCC Co facets. At 1/4 ML, CO prefers to adsorb at the top, bridge, hollow, and B_5 sites over (100), (110), (111), and (311) facets in FCC Co, respectively. By increasing CO coverage from 1/4 to 1/2 ML, CO migrates from the top site to bridge site on (100) surface, whereas CO molecules begin to adsorb extra horizontally on (110) surface and at the top and B_5 sites on (311) surface. As CO coverage increases further to 1 ML, CO molecules prefer to adsorb at the bridge sites, forming zigzag patterns on all FCC Co facets except for (111) surface where the 3-fold hollow site is more favorable for CO adsorption. CO adsorbs on FCC Co facets in such a way to maximize the usage of the surface area and minimize the repulsive interactions among the adjacent adsorbed CO molecules. Different motifs of CO adsorption configurations can be found over distinct FCC Co facets because of their different surface topologies (Figure 1 and Figure S1).

The average CO adsorption energies are surface coverages dependent. At a low coverage 1/4 ML (Figure 1), the calculated average CO adsorption energy on FCC Co is −1.69 eV, which is at least 0.23 eV lower than the experimental measured CO adsorption enthalpy of −1.25 to −1.46 eV.[61] This mainly comes from the overestimation of CO adsorption strength by DFT calculations using PBE functionals.[62,63] CO usually adsorbs stronger on the open (311) surfaces than on the flat (100) and (111) surfaces regardless of the variations of CO coverage. Specifically, at 1/4 ML, the calculated CO adsorption energies are −1.69, −1.61, −1.69, and −1.61 eV on (311), (110), (100), and (111) surfaces, respectively. As CO coverage increases, the average CO adsorption strength increase by 0.11 and 0.09 eV at 1/2 ML on the open (110) and (311) surfaces, respectively, but then their values decrease to −1.59 and −1.64 eV at 1 ML. Nevertheless, the CO adsorption strength decreases gradually to −0.96 eV on the (100) surface and −0.57 eV on the (111) surface with CO coverage increasing from 1/4 to 1 ML (Figure S1). The surface

https://dx.doi.org/10.1021/acs.jpcc.0c07386
J. Phys. Chem. C XXXX, XXX, XXX−XXX

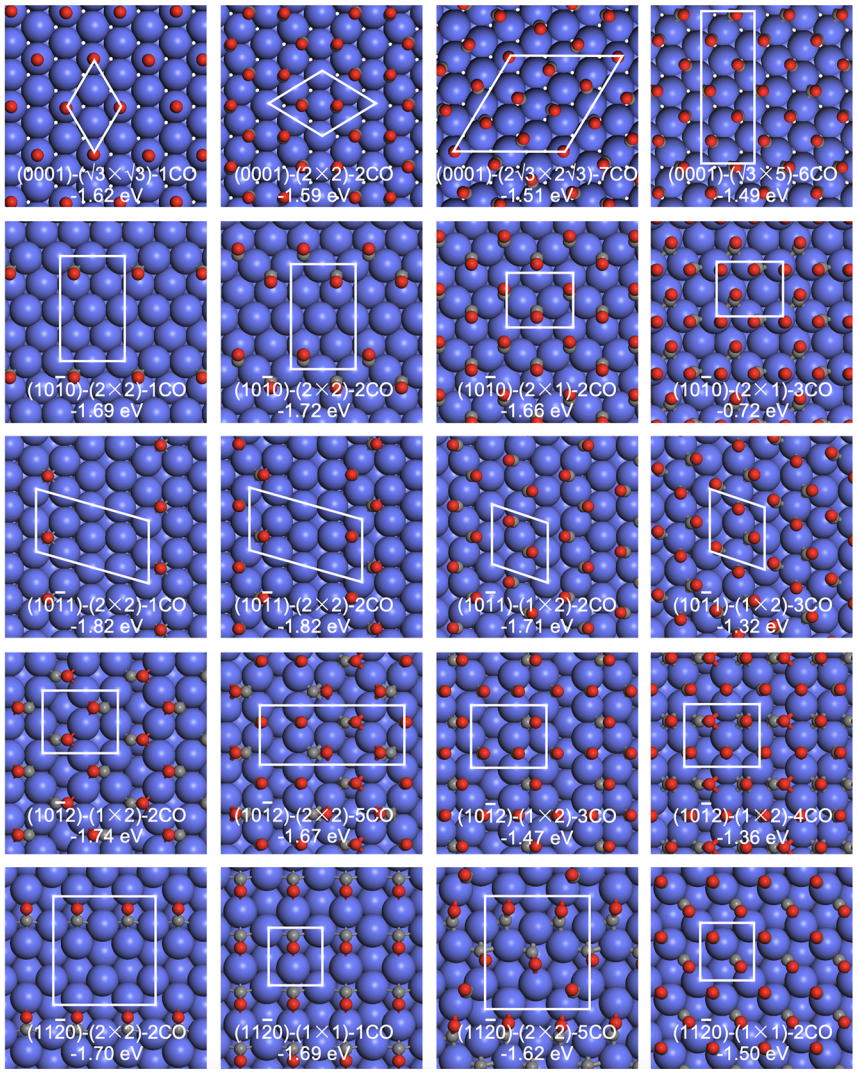

Figure 2. Optimized CO adsorption configurations and corresponding average adsorption energies (eV) at different coverages over HCP Co facets.

coverage effect of CO adsorption among different facets is discussed in more detail below.

As compared with FCC Co, HCP Co exposes more open and corrugated surfaces due to the symmetry requirement of the D_{6h} point group. More possible CO adsorption sites are taken into account to identify the most favorable CO adsorption structures on HCP Co facets. CO adsorbs stronger on HCP Co as compared to FCC Co. For example, at 1/4 ML coverage (Figure 2 and Figure S2), the average CO adsorption energy is −1.72 eV, which is 0.07 eV lower than that on FCC Co. CO prefers to adsorb at the top, 3-fold, 4-fold, 4-fold, and ridge bridge sites on the five (0001), (10$\bar{1}$0), (10$\bar{1}$1), (10$\bar{1}$2), and (11$\bar{2}$0) facets, respectively. Our calculated CO adsorption configurations and energies are consistent with previous theoretical reports for CO adsorption on the {0001} surface at low coverages of 1/4 and 1/3 ML, the {10$\bar{1}$2} surface at 1/2 ML, and the {11$\bar{2}$0} surface at 1 ML.[64,65] As the CO coverage increases from 1/4 to 1/2 ML, the HCP-hollow sites are more favorable for CO adsorption on (0001), while CO adsorbs at the 3-fold and/or 4-fold sites forming a zigzag pattern on (10$\bar{1}$0), (10$\bar{1}$1), and (10$\bar{1}$2) facets and also CO adsorbs stable at the B_S sites on the (11$\bar{2}$0) facet. The bridge/3-fold sites are more preferable for CO adsorption at 1 ML on all HCP Co facets except for the (10$\bar{1}$2) facet where CO molecules adsorb stable at the 4-fold site horizontally and further sink into surface trenches on the (11$\bar{2}$0) facet. As CO coverages increase larger than 1 ML, CO adsorption at the top and bridge sites nearby becomes more frequent.

Average CO adsorption energies are still determined by surface coverages and surface structures of HCP Co. At 1/4 ML, average CO adsorption energies of the corrugated (10$\bar{1}$0), (10$\bar{1}$2), and (11$\bar{2}$0) surfaces are similar to the values of −1.69, −1.76, and −1.63 eV, respectively. As the CO coverage increases, CO adsorption strength first increases by 0.03, 0.00, and 0.07 eV at 1/2 ML and then decreases to −1.66, −1.74, and −1.69 eV further at 1 ML on these three corrugated surfaces, respectively. When the CO coverage increases higher than 1 ML, the repulsive interaction between neighboring CO molecules becomes more significant. As a result, the average CO adsorption energies will sharply increase to −1.25 eV at 1.33 ML and −0.72 eV at 1.5 ML on (10$\bar{1}$0), −1.29 eV at 2 ML and −0.82 eV at 2.5 ML on (10$\bar{1}$2), and −0.94 eV at 2.5 ML and −0.73 eV at 3 ML on the (11$\bar{2}$0) facet. Whereas for the remaining (0001) and (10$\bar{1}$1) facets, the CO adsorption strength decreases gradually from −1.62 to −0.57 eV and from −1.82 to −1.71 eV with CO coverage increasing from 1/4 to 1 ML, respectively, and will continue increasing to −0.73 when the CO coverage reaches 2 ML on (10$\bar{1}$1). More experimental

https://dx.doi.org/10.1021/acs.jpcc.0c07386
J. Phys. Chem. C XXXX, XXX, XXX−XXX

works on CO adsorption over single crystals are desirable to corroborate our theoretical predictions of CO adsorption energies trend and configurations over various FCC Co and HCP Co facets under different CO exposures.

Additionally, we have also examined some extra ordered structures, such as $(\sqrt{3} \times \sqrt{3})R30°$-CO (1/3 ML), $c(4 \times 2)$-4CO (1/2 ML), $(2\sqrt{3} \times 2\sqrt{3})R30°$-7CO (7/12 ML), $c(\sqrt{3} \times 5)$rect-6CO (6/10 ML), and $c(\sqrt{3} \times 3)$rect-4CO (4/6 ML) structures (Figures S1 and S2) which were observed experimentally on Co close-packed flat (111) and (0001) facets as well as on many other metals under different CO exposures.[66−68] Our theoretically predicted most stable CO adsorption configurations are consistent with the experimental identified $(\sqrt{3} \times \sqrt{3})R30°$-CO, $(2\sqrt{3} \times 2\sqrt{3})R30°$-7CO, and $c(\sqrt{3} \times 3)$rect-4CO structures where CO molecules prefer to adsorb all at top sites, 1CO at top and 6 CO molecules at bridge sites, and at top and bridge sites with a ratio of 3:1, respectively.[69,70] Whereas for the $c(4 \times 2)$-4CO structure, Biberrian et al. reported that CO adsorbs equally populated at the bridge and top sites;[71,72] however, our calculations indicate that the average CO adsorption energy of the same structure is 0.05 eV higher than that of (2×2)-2CO hexagonal ring patterns as we found. Therefore, (2×2)-2CO hexagonal ring structure is slightly more stable than a mighty minima $c(4 \times 2)$-4CO structure, and both structures can coexist. There are four top and two bridge CO molecules composed of $c(\sqrt{3} \times 5)$rect-6CO structure proposed by Avery and Persson et al. (Figure S2).[73,74] However, our calculation shows that $c(\sqrt{3} \times 5)$rect-6CO with all CO molecules locating at the bridge is more stable by −0.14 eV per CO. Our DFT calculations are comparable with the experimental measurements and can successfully predict new CO adsorption configurations.

CO Coverage Effect. To describe the interactions of CO molecules on different FCC and HCP Co facets, we use another format of CO coverage θ here being the number of adsorbed CO molecules on a surface with an area of A_S, in units of Å^{-2}.

The variation of E_{ad} as a function of θ is a key factor to understand CO adsorption behavior on FCC Co and HCP Co facets, as depicted in Figure 3. The fitted polynomial function is expressed best by $E_{ad} = a + b \times \theta^2 + c \times \theta^3$, where a, b, and c are the fitting parameters.[75,76] As shown in Figure 3, it is obvious that the average CO adsorption energy first decreases and then increases quickly on various FCC and HCP Co facets with increasing CO coverage. The interactions between the adjacent CO molecules are first attractive at low coverage, which might come from long-range van der Waals interaction between adsorbed CO molecules and the interaction mediated by the substrate. Whereas the electrostatic repulsive interaction takes control at high CO coverage. At the relatively low coverage region ($0 < \theta < 0.08$ Å^{-2}), there is visible energy difference between HCP Co and FCC Co, which clearly tells that CO adsorbs stronger on HCP Co than FCC Co. The reason can be attributed to the fact that HCP Co exposes more open surfaces and more coordinate-unsaturated sites than FCC Co. However, as CO coverage increases ($\theta > 0.12$ Å^{-2}), the two adsorption lines for HCP Co and FCC Co coincident eventually (Figure S3). In other words, the structure sensitivity of CO adsorption on HCP Co and FCC Co facets would decrease with the increase of CO coverage due to the overwhelming repulsion between CO adsorbates.

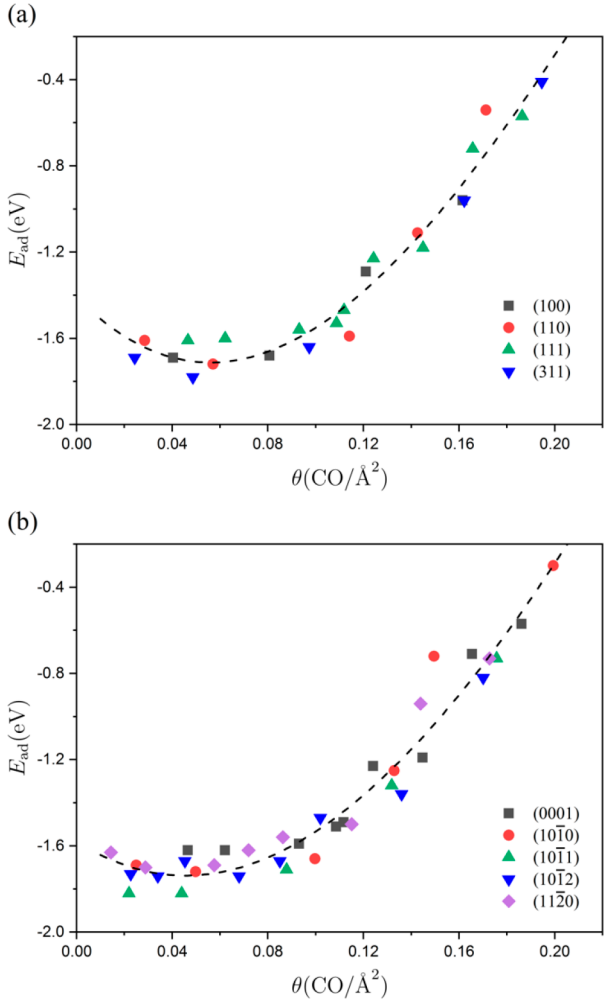

Figure 3. Average CO adsorption energies as a function of CO coverages θ over FCC Co (a) and HCP Co (b) facets.

Surface Energy Diagram. The overall surface free energy of a specific FCC Co and HCP Co facet can be calculated by summation of the bare surface energy and Gibbs free energy change of CO adsorption (eq 2). To compare the relative stability of various CO adsorption configurations at different CO atmospheres, the surface energy diagrams of FCC Co and HCP Co facets were plotted as a function of CO chemical potential. Two exemplary surface free energy diagrams of FCC (311) and HCP (10$\bar{1}$2) facets dependent on CO chemical potential are presented in Figure 4. Each line represents a CO adsorption structure, and the different slopes of each line represent different CO adsorption coverages in Figure 4. The horizontal dashed lines correspond to their clean surface energies without the presence of CO. FCC (311) and HCP (10$\bar{1}$2) surfaces are selected and shown here based on the criteria that they have similar clean surface energy, and they are the most abundant corrugated facets exposed in the corresponding Wulff shapes of FCC Co and HCP Co in the presence of CO (Figures 5 and 6), respectively. The envelope bold lines inside are the most stable CO adsorption configurations with the variation of CO chemical potentials. The surface energy diagram as a function of CO chemical potentials can be divided into four regimes: the bare surface, the onset of CO adsorption, low CO coverage structures, and high CO coverage structures. It is obvious that the surface free

https://dx.doi.org/10.1021/acs.jpcc.0c07386
J. Phys. Chem. C XXXX, XXX, XXX−XXX

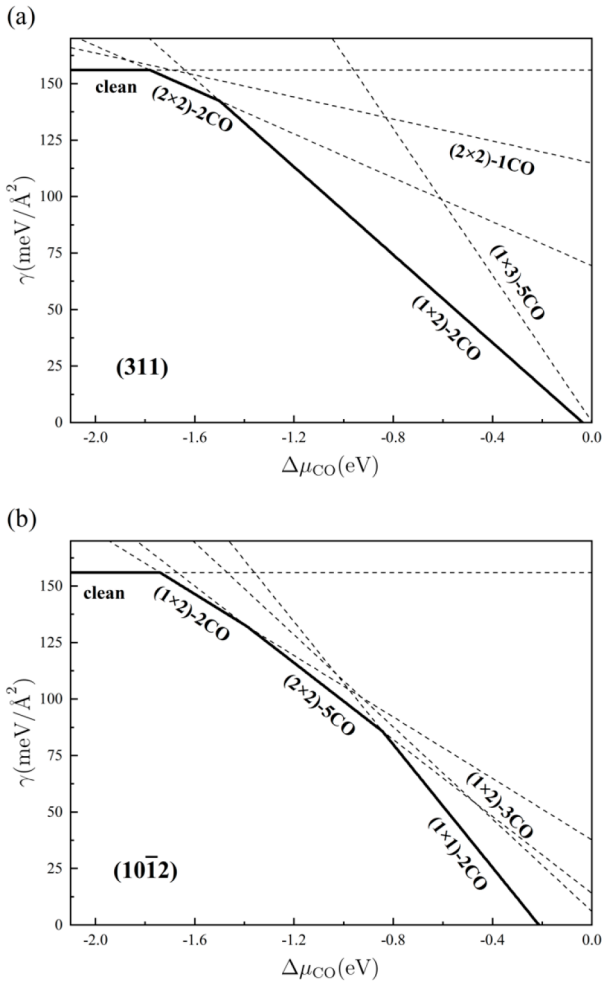

Figure 4. Surface free energy diagram of FCC Co (311) (a) and HCP Co (10$\bar{1}$2) and (b) facets as a function of CO chemical potential.

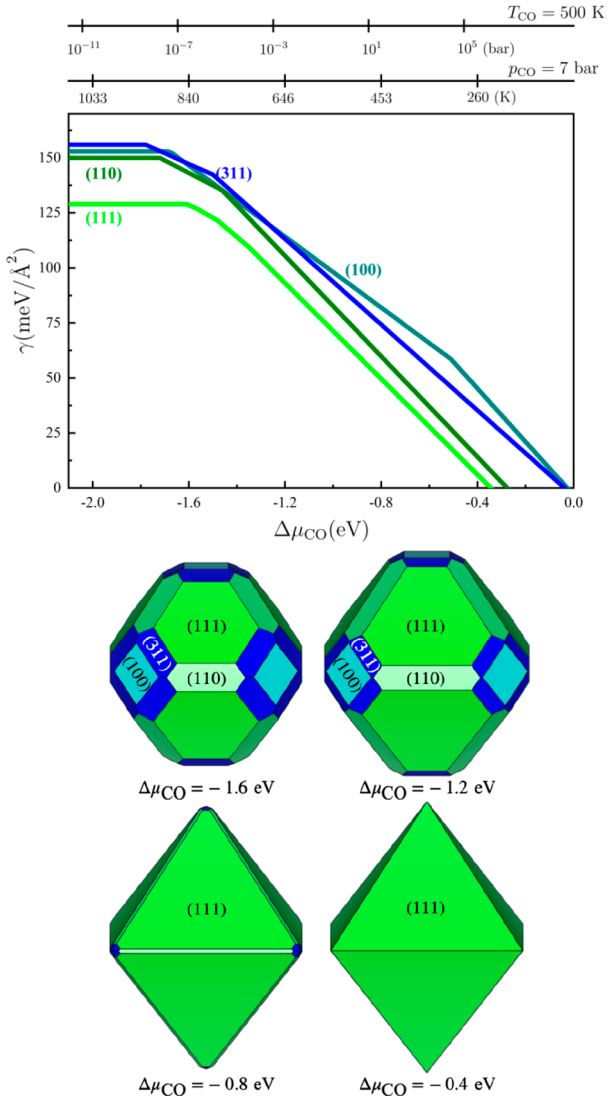

Figure 5. Phase diagram of FCC Co as a function of CO chemical potential and FCC Co Wulff morphologies at $\Delta\mu_{CO}$ = −1.6, −1.2, −0.8, and −0.4 eV. CO chemical potentials as a function of temperature (P_{CO} = 7 bar) or CO pressure (T = 500 K) are indicated.

energies of both FCC (311) and HCP (10$\bar{1}$2) surfaces decrease as CO chemical potential increases.

Morphology of FCC and HCP Co under a CO Atmosphere. We now turn to discuss the influence of CO chemical potential on the morphologies of FCC Co and HCP Co. From above, the most favorable CO adsorption configuration on each facet of FCC Co and HCP Co is used to derive the corresponding surface energy diagrams of FCC Co and HCP Co as a function of CO chemical potential. The thermodynamic equilibrium morphological shapes of FCC Co and HCP Co can be obtained via Wulff construction based on the calculated surface free energies (Figures 5 and 6).

As mentioned above, all the surface free energies would be reduced by CO adsorption, which has a great influence on the relatively stabilities of FCC Co and HCP Co facets in turn. When CO chemical potential increases, the surface free energy of each facet in FCC Co decreases in different degrees, implying that the relatively stabilities of different FCC Co facets are strongly dependent on CO chemical potentials. As CO chemical potential increases from −2.0 to −1.6 eV, the surface area proportions of {110} and {311} facets increase accompanied by decreasing that of {100} and {111} facets, but the most abundant exposed facets are always {111}. Our previous work showed that {311}, {110}, and {100} facets have similar high CO activation rates, and the {111} surface has the lowest activity for CO activation in FCC Co.[40] All the three highly active {311}, {110}, and {100} facets, which dominate the CO activation rate, can be exposed in the Wulff shape of FCC Co at $\Delta\mu_{CO}$ below −1.2 eV. However, {311}, {110}, and {100} facets decrease or even disappear, and the surface area of {111} facets increase continuously with increasing CO chemical potential further to −0.80 eV. In the high CO chemical potential area ($\Delta\mu_{CO}$ > −0.8 eV), the Wulff shape of FCC Co becomes an octahedron occupied by nearly all {111} surfaces. This kind of shape is usually synthesized by hydrothermal experiments through certain kinds of surface ligands used in Au, Ag, and Co nanocatalysts by tuning their surface energies.[77−82] Our theoretical predictions are consistent with the previous theoretical report that the most exposed surface of FCC Co is always {111} regardless of the CO chemical potential. However, the {311} surface can present in FCC Co shape in our work when the CO chemical potential is below −1.2 eV, which is different from Hou's report.[83] This can be attributed to the fact that more stable CO adsorption configurations were identified in our present work. Additionally, future works should focus on {311}, {100},

https://dx.doi.org/10.1021/acs.jpcc.0c07386
J. Phys. Chem. C XXXX, XXX, XXX−XXX

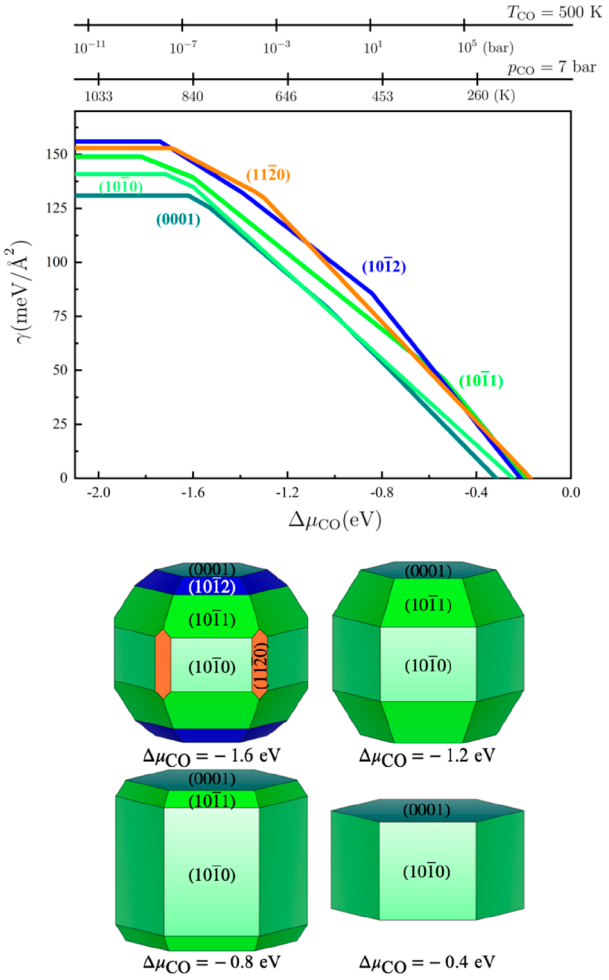

Figure 6. Phase diagram of HCP Co as a function of CO chemical potential and HCP Co Wulff morphologies at $\Delta\mu_{CO}$ = −1.6, −1.2, −0.8, and −0.4 eV. CO chemical potentials as a function of temperature (P_{CO} = 7 bar) or CO pressure (T = 500 K) are indicated.

{110}, and {111} facets at a high CO coverage (−1.6 eV < $\Delta\mu_{CO}$ < −0.8 eV), which would be important for FTS.

Different from FCC Co, HCP Co has a dihedral-like shape under vacuum conditions, and {0001}, {10$\bar{1}$0}, and {10$\bar{1}$1} facets dominate the total surface area of HCP Co by 72% at least. The crystal symmetry of HCP Co requires its morphology to be maintained in hexagonal double cones. Similar to FCC Co, the surface free energy of a specific HCP Co facet decreases as CO chemical potential increases. To visualize the morphology evolution of HCP Co nanoparticles induced by CO, all the constructed Wulff morphologies have been summarized and are displayed in Figure 6. Upon CO adsorption, the proportion of HCP Co {0001} surface does not change greatly, which is mainly attributed to its highest thermodynamic stability derived from its lowest surface free energy. At a low CO coverage ($\Delta\mu_{CO}$ = −2.0 eV), the fraction of each surface in HCP Co Wulff shape changes slightly with respect to that of the HCP Co under vacuum conditions. When the CO chemical potential increases from −2.0 to −1.6 eV, the surface area proportions of {10$\bar{1}$2} and {10$\bar{1}$1} facets increases slightly from 13% and 36% to 16% and 41% at the expense of {10$\bar{1}$0}, {0001}, and {11$\bar{2}$0} ones, respectively. Therefore, CO dissociation activity might be slightly enhanced by increasing CO chemical potential below −1.6 eV due to the exposure of denser active sites residing on the {10$\bar{1}$2} and {10$\bar{1}$1} facets which are highly active in HCP Co. In particular, when increasing CO chemical potential further to −1.2 eV, the fraction of {10$\bar{1}$2} and {11$\bar{2}$0} surface disappears, while {10$\bar{1}$0} increases sharply in HCP Co shape. Later, only {0001}, {10$\bar{1}$0}, and a small fraction of {10$\bar{1}$1} facets can be exposed in HCP Co Wulff shape when the CO chemical potential increases up to −0.8 eV. In other words, the surface area proportions of highly active {10$\bar{1}$1} and {10$\bar{1}$2} facets decrease as CO chemical potential increases from −1.6 to −0.8 eV. More theoretical and experimental works should focus on the CO covered {10$\bar{1}$1}, {10$\bar{1}$2}, and {11$\bar{2}$0} facets which may be exposed in HCP Co Wulff shape at a moderate CO chemical potential (−1.6 eV < $\Delta\mu_{CO}$ < −0.8 eV). It is interesting to point out that in a high CO chemical potential area ($\Delta\mu_{CO}$ > −0.4 eV), the Wulff shape of FCC Co becomes an hexagonal prism occupied by six {10$\bar{1}$0} and capped by two {0001} surfaces. This kind of shape is usually synthesized by hydrothermal experiment through certain kinds of surface ligands as used in Pd, Ag, Pt, and Co nanocatalysts by tuning their surface energies.[84,85]

Our previous work showed that there is a compensation effect between the surface energy and the bulk energy, which provides a driving force for the size-induced phase transition of the nanoparticles.[32] CO adsorption on nanoparticles will change the surface free energy difference between HCP Co and FCC Co due to the structure sensitivity of CO adsorption, as shown in Figure 7. As compared with FCC Co and HCP Co

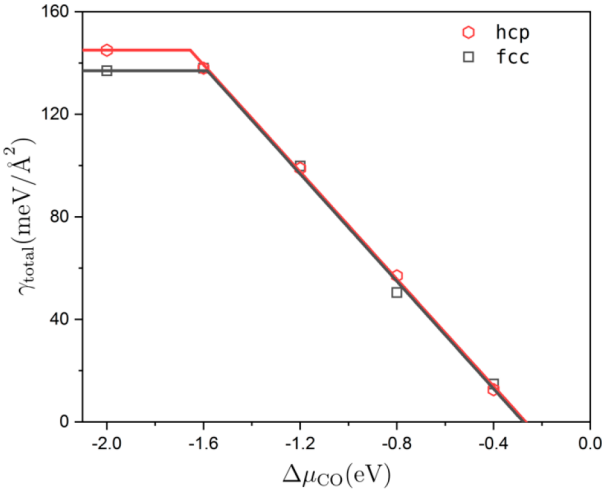

Figure 7. Total surface free energy of HCP Co and FCC Co as a function of CO chemical potential.

in vacuum conditions, the surface free energy difference between FCC Co and HCP Co is almost diminished with the introduction of CO adsorption at a high CO chemical potential. This can be originated from the less structure sensitivity of CO adsorption over HCP Co and FCC Co at higher coverage. Therefore, the crystal phase transformation between HCP Co and FCC Co is in general hindered under a CO atmosphere.

CONCLUSION

The surface structures, stabilities, and equilibrium morphologies of FCC Co and HCP Co induced by CO adsorption were studied by *ab initio* thermodynamics. It is found that on both

https://dx.doi.org/10.1021/acs.jpcc.0c07386
J. Phys. Chem. C XXXX, XXX, XXX−XXX

FCC Co and HCP Co the CO adsorption strength first increases with lateral attraction between adsorbed CO and then quickly decreases due to developed lateral repulsion as CO chemical potential increases. Because the repulsive lateral interaction between adsorbed CO is dominating at high CO coverage, the CO adsorption strength on average becomes insensitive to the Co crystal phases. Similar to the Wulff shape of FCC Co under vacuum conditions, open {311}, {100}, and {110} facets can be exposed in FCC Co at a moderate CO chemical potential. Whereas FCC Co has an octahedron shape occupied by nearly all {111} facets at a high CO chemical potential, and the $\{10\bar{1}1\}$, $\{10\bar{1}2\}$, and $\{11\bar{2}0\}$ facets dominate the HCP Co Wulff shape under moderate CO chemical potential conditions. The morphology of HCP Co is covered by $\{10\bar{1}0\}$ and {0001} facets at a high CO chemical potential. Future work should focus on these most probable facets in FCC Co and HCP Co under CO atmospheres. The nearly diminished difference between FCC Co and HCP Co induced by CO adsorption might influence the crystal phase transformation between them at small particle size, given that activity is strongly related to its structure and phase, which will have great importance on their catalytic performance as a result.

■ ASSOCIATED CONTENT

Supporting Information

The Supporting Information is available free of charge at https://pubs.acs.org/doi/10.1021/acs.jpcc.0c07386.

Optimized CO adsorption configurations and average CO adsorption energies (Figures S1 and S2); average CO adsorption energies as a function of CO coverages (Figure S3) (PDF)

■ AUTHOR INFORMATION

Corresponding Authors

Wei-Xue Li − *Department of Chemical Physics, School of Chemistry and Materials Science and Hefei National Laboratory for Physical Science at the Microscale, University of Science and Technology of China, Hefei 230026, China;* orcid.org/0000-0002-5043-3088; Email: wxli70@ustc.edu.cn

Hong-Jun Fan − *State Key Laboratory of Molecular Reaction Dynamics, Dalian Institute of Chemical Physics, Chinese Academy of Sciences, Dalian 116023, China;* orcid.org/0000-0003-3406-6932; Email: fanhj@dicp.ac.cn

Authors

Hao Lin − *State Key Laboratory of Molecular Reaction Dynamics, Dalian Institute of Chemical Physics, Chinese Academy of Sciences, Dalian 116023, China; University of Chinese Academy of Sciences, Beijing 100049, China*

Jin-Xun Liu − *Department of Chemical Physics, School of Chemistry and Materials Science, University of Science and Technology of China, Hefei 230026, China;* orcid.org/0000-0002-7499-4197

Complete contact information is available at: https://pubs.acs.org/10.1021/acs.jpcc.0c07386

Author Contributions

H.L. and J.-X.L. contributed equally to this work.

Notes

The authors declare no competing financial interest.

■ ACKNOWLEDGMENTS

This work was supported by the National Natural Science Foundation of China (91645202, 91945302), the Key Technologies R&D Program of China (2017YFB0602205, 2018YFA0208603), and the Chinese Academy of Sciences Key Project (QYZDJ-SSW-SLH054). The Super Computing Center of USTC is gratefully acknowledged.

■ REFERENCES

(1) Zheng, N.; Stucky, G. D. A General Synthetic Strategy for Oxide-Supported Metal Nanoparticle Catalysts. *J. Am. Chem. Soc.* **2006**, *128*, 14278−14280.

(2) Murphy, C. J.; Sau, T. K.; Gole, A. M.; Orendorff, C. J.; Gao, J.; Gou, L.; Hunyadi, S. E.; Li, T. Anisotropic Metal Nanoparticles: Synthesis, Assembly, and Optical Applications. *J. Phys. Chem. B* **2005**, *109*, 13857−13870.

(3) Wang, J.; Chen, H.; Hu, Z.; Yao, M.; Li, Y. A Review on the Pd-Based Three-Way Catalyst. *Catal. Rev.: Sci. Eng.* **2015**, *57*, 79−144.

(4) Davis, S. E.; Ide, M. S.; Davis, R. J. Selective Oxidation of Alcohols and Aldehydes over Supported Metal Nanoparticles. *Green Chem.* **2013**, *15*, 17−45.

(5) Xia, Y.; Xiong, Y.; Lim, B.; Skrabalak, S. E. Shape-Controlled Synthesis of Metal Nanocrystals: Simple Chemistry Meets Complex Physics? *Angew. Chem., Int. Ed.* **2009**, *48*, 60−103.

(6) Jia, C.-J.; Schüth, F. Colloidal Metal Nanoparticles as a Component of Designed Catalyst. *Phys. Chem. Chem. Phys.* **2011**, *13*, 2457−2487.

(7) Van Santen, R. A. Complementary Structure Sensitive and Insensitive Catalytic Relationships. *Acc. Chem. Res.* **2009**, *42*, 57−66.

(8) Hansen, P. L.; Wagner, J. B.; Helveg, S.; Rostrup-Nielsen, J. R.; Clausen, B. S.; Topsøe, H. Atom-Resolved Imaging of Dynamic Shape Changes in Supported Copper Nanocrystals. *Science* **2002**, *295*, 2053.

(9) Uchiyama, T.; Yoshida, H.; Kuwauchi, Y.; Ichikawa, S.; Shimada, S.; Haruta, M.; Takeda, S. Systematic Morphology Changes of Gold Nanoparticles Supported on CeO_2 During Co Oxidation. *Angew. Chem., Int. Ed.* **2011**, *50*, 10157−10160.

(10) Tao, F.; Dag, S.; Wang, L.-W.; Liu, Z.; Butcher, D. R.; Salmeron, M.; Somorjai, G. A. Restructuring of Hex-Pt(100) under Co Gas Environments: Formation of 2-D Nanoclusters. *Nano Lett.* **2009**, *9*, 2167−2171.

(11) Yoshida, H.; Kuwauchi, Y.; Jinschek, J. R.; Sun, K.; Tanaka, S.; Kohyama, M.; Shimada, S.; Haruta, M.; Takeda, S. Visualizing Gas Molecules Interacting with Supported Nanoparticulate Catalysts at Reaction Conditions. *Science* **2012**, *335*, 317.

(12) Wittig, J. E.; Bentley, J.; Allard, L. F. In Situ Investigation of Ordering Phase Transformations in FePt Magnetic Nanoparticles. *Ultramicroscopy* **2017**, *176*, 218−232.

(13) Tao, F.; Salmeron, M. In Situ Studies of Chemistry and Structure of Materials in Reactive Environments. *Science* **2011**, *331*, 171−174.

(14) Bañares, M. A. Operando Methodology: Combination of in Situ Spectroscopy and Simultaneous Activity Measurements under Catalytic Reaction Conditions. *Catal. Today* **2005**, *100*, 71−77.

(15) Grajciar, L.; Heard, C. J.; Bondarenko, A. A.; Polynski, M. V.; Meeprasert, J.; Pidko, E. A.; Nachtigall, P. Towards Operando Computational Modeling in Heterogeneous Catalysis. *Chem. Soc. Rev.* **2018**, *47*, 8307−8348.

(16) Van de Loosdrecht, J.; Botes, F.; Ciobica, I.; Ferreira, A.; Gibson, P.; Moodley, D.; Saib, A.; Visagie, J.; Weststrate, C.; Niemantsverdriet, J. Fischer−Tropsch Synthesis: Catalysts and Chemistry. In *Comprehensive Inorganic Chemistry II: From Elements to Applications*; Elsevier: 2013; pp 525−557.

(17) Röper, M. Fischer−Tropsch Synthesis. In *Catalysis in C1 Chemistry*; Keim, W., Ed.; Springer Netherlands: Dordrecht, 1983; pp 41−88.

(18) Biloen, P.; Sachtler, W. M. H.; Eley, D. D.; Pines, H.; Weisz, P. B. Mechanism of Hydrocarbon Synthesis over Fischer−Tropsch Catalysts. *Adv. Catal.* **1981**, *30*, 165−l216.

(19) Schulz, H.; Davis, B. H.; Occelli, M. L. Comparing Fischer–Tropsch Synthesis on Iron- and Cobalt Catalysts: The Dynamics of Structure and Function. *Stud. Surf. Sci. Catal.* **2007**, *163*, 177–199.
(20) Iglesia, E.; Soled, S. L.; Fiato, R. A.; Via, G. H. Bimetallic Synergy in Cobalt Ruthenium Fischer–Tropsch Synthesis Catalysts. *J. Catal.* **1993**, *143*, 345–368.
(21) Dry, M. E.; Hoogendoorn, J. C. Technology of the Fischer–Tropsch Process. *Catal. Rev.: Sci. Eng.* **1981**, *23*, 265–278.
(22) Khodakov, A. Y.; Chu, W.; Fongarland, P. Advances in the Development of Novel Cobalt Fischer–Tropsch Catalysts for Synthesis of Long-Chain Hydrocarbons and Clean Fuels. *Chem. Rev.* **2007**, *107*, 1692–1744.
(23) Zhang, Q.; Kang, J.; Wang, Y. Development of Novel Catalysts for Fischer–Tropsch Synthesis: Tuning the Product Selectivity. *ChemCatChem* **2010**, *2*, 1030–1058.
(24) Reuel, R. C.; Bartholomew, C. H. Effects of Support and Dispersion on the Co Hydrogenation Activity/Selectivity Properties of Cobalt. *J. Catal.* **1984**, *85*, 78–88.
(25) Bezemer, G. L.; Bitter, J. H.; Kuipers, H. P. C. E.; Oosterbeek, H.; Holewijn, J. E.; Xu, X.; Kapteijn, F.; van Dillen, A. J.; de Jong, K. P. Cobalt Particle Size Effects in the Fischer–Tropsch Reaction Studied with Carbon Nanofiber Supported Catalysts. *J. Am. Chem. Soc.* **2006**, *128*, 3956–3964.
(26) Barbier, A.; Tuel, A.; Arcon, I.; Kodre, A.; Martin, G. A. Characterization and Catalytic Behavior of Co/SiO_2 Catalysts: Influence of Dispersion in the Fischer–Tropsch Reaction. *J. Catal.* **2001**, *200*, 106–116.
(27) Martínez, A.; Prieto, G. Breaking the Dispersion-Reducibility Dependence in Oxide-Supported Cobalt Nanoparticles. *J. Catal.* **2007**, *245*, 470–476.
(28) den Breejen, J. P.; Radstake, P. B.; Bezemer, G. L.; Bitter, J. H.; Frøseth, V.; Holmen, A.; de Jong, K. P. On the Origin of the Cobalt Particle Size Effects in Fischer–Tropsch Catalysis. *J. Am. Chem. Soc.* **2009**, *131*, 7197–7203.
(29) Xiong, H.; Motchelaho, M. A. M.; Moyo, M.; Jewell, L. L.; Coville, N. J. Correlating the Preparation and Performance of Cobalt Catalysts Supported on Carbon Nanotubes and Carbon Spheres in the Fischer–Tropsch Synthesis. *J. Catal.* **2011**, *278*, 26–40.
(30) Kitakami, O.; Sato, H.; Shimada, Y.; Sato, F.; Tanaka, M. Size Effect on the Crystal Phase of Cobalt Fine Particles. *Phys. Rev. B: Condens. Matter Mater. Phys.* **1997**, *56*, 13849–13854.
(31) Andreev, A. S.; d'Espinose de Lacaillerie, J.-B.; Lapina, O. B.; Gerashenko, A. Thermal Stability and HCP–FCC Allotropic Transformation in Supported Co Metal Catalysts Probed near Operando by Ferromagnetic NMR. *Phys. Chem. Chem. Phys.* **2015**, *17*, 14598–14604.
(32) Lin, H.; Liu, J.-X.; Fan, H.; Li, W.-X. Compensation between Surface Energy and HCP/FCC Phase Energy of Late Transition Metals from First-Principles Calculations. *J. Phys. Chem. C* **2020**, *124*, 11005–11014.
(33) Liang, S.; Teng, F.; Bulgan, G.; Zong, R.; Zhu, Y. Effect of Phase Structure of MnO_2 Nanorod Catalyst on the Activity for Co Oxidation. *J. Phys. Chem. C* **2008**, *112*, 5307–5315.
(34) Chen, Y.; Lai, Z.; Zhang, X.; Fan, Z.; He, Q.; Tan, C.; Zhang, H. Phase Engineering of Nanomaterials. *Nat. Rev. Chem.* **2020**, *4*, 243–256.
(35) Zhao, M.; Xia, Y. Crystal-Phase and Surface-Structure Engineering of Ruthenium Nanocrystals. *Nat. Rev. Mater.* **2020**, *5*, 440–459.
(36) Zhang, B.-Y.; Su, H.-Y.; Liu, J.-X.; Li, W.-X. Interplay between Site Activity and Density of Bcc Iron for Ammonia Synthesis Based on First-Principles Theory. *ChemCatChem* **2019**, *11*, 1928–1934.
(37) Liu, J.-X.; Li, W.-X. Theoretical Study of Crystal Phase Effect in Heterogeneous Catalysis. *WIREs Comput. Mol. Sci.* **2016**, *6*, 571–583.
(38) Ducreux, O.; Rebours, B.; Lynch, J.; Roy-Auberger, M.; Bazin, D. Microstructure of Supported Cobalt Fischer–Tropsch Catalysts. *Oil Gas Sci. Technol.* **2009**, *64*, 49–62.
(39) Enache, D. I.; Rebours, B.; Roy-Auberger, M.; Revel, R. In Situ XRD Study of the Influence of Thermal Treatment on the Characteristics and the Catalytic Properties of Cobalt-Based Fischer–Tropsch Catalysts. *J. Catal.* **2002**, *205*, 346–353.
(40) Liu, J.-X.; Su, H.-Y.; Sun, D.-P.; Zhang, B.-Y.; Li, W.-X. Crystallographic Dependence of Co Activation on Cobalt Catalysts: HCP Versus FCC. *J. Am. Chem. Soc.* **2013**, *135*, 16284–16287.
(41) Nie, L.; Li, Z.; Kuang, T.; Lyu, S.; Liu, S.; Zhang, Y.; Peng, B.; Li, J.; Wang, L. Role of Well-Defined Cobalt Crystal Facets in Fischer–Tropsch Synthesis: A Combination of Experimental and Theoretical Studies. *Chem. Commun.* **2019**, *55*, 10559–10562.
(42) Zhang, R.; Kang, L.; Liu, H.; Wang, B.; Li, D.; Fan, M. Crystal Facet Dependence of Carbon Chain Growth Mechanism over the HCP and FCC Co Catalysts in the Fischer–Tropsch Synthesis. *Appl. Catal., B* **2020**, *269*, 118847.
(43) Gnanamani, M. K.; Jacobs, G.; Shafer, W. D.; Davis, B. H. Fischer–Tropsch Synthesis: Activity of Metallic Phases of Cobalt Supported on Silica. *Catal. Today* **2013**, *215*, 13–17.
(44) Kresse, G.; Hafner, J. Ab Initio Molecular-Dynamics Simulation of the Liquid-Metal–Amorphous-Semiconductor Transition in Germanium. *Phys. Rev. B: Condens. Matter Mater. Phys.* **1994**, *49*, 14251–14269.
(45) Kresse, G.; Furthmüller, J. Efficient Iterative Schemes for Ab Initio Total-Energy Calculations Using a Plane-Wave Basis Set. *Phys. Rev. B: Condens. Matter Mater. Phys.* **1996**, *54*, 11169–11186.
(46) Kresse, G.; Furthmüller, J. Efficiency of Ab-Initio Total Energy Calculations for Metals and Semiconductors Using a Plane-Wave Basis Set. *Comput. Mater. Sci.* **1996**, *6*, 15–50.
(47) Blöchl, P. E. Projector Augmented-Wave Method. *Phys. Rev. B: Condens. Matter Mater. Phys.* **1994**, *50*, 17953–17979.
(48) Kresse, G.; Joubert, D. From Ultrasoft Pseudopotentials to the Projector Augmented-Wave Method. *Phys. Rev. B: Condens. Matter Mater. Phys.* **1999**, *59*, 1758–1775.
(49) Perdew, J. P.; Burke, K.; Ernzerhof, M. Generalized Gradient Approximation Made Simple. *Phys. Rev. Lett.* **1996**, *77*, 3865–3868.
(50) Perdew, J. P.; Burke, K.; Ernzerhof, M. Generalized Gradient Approximation Made Simple [Phys. Rev. Lett. 77, 3865 (1996)]. *Phys. Rev. Lett.* **1997**, *78*, 1396–1396.
(51) Methfessel, M.; Paxton, A. T. High-Precision Sampling for Brillouin-Zone Integration in Metals. *Phys. Rev. B: Condens. Matter Mater. Phys.* **1989**, *40*, 3616–3621.
(52) Davidson, E. In *Methods in Computational Molecular Physics*; NATO Advanced Study Institute, Series C: Plenum: New York, 1983; p 95.
(53) Monkhorst, H. J.; Pack, J. D. Special Points for Brillouin-Zone Integrations. *Phys. Rev. B* **1976**, *13*, 5188–5192.
(54) Reuter, K.; Stampf, C.; Scheffler, M. Ab Initio Atomistic Thermodynamics and Statistical Mechanics of Surface Properties and Functions. In *Handbook of Materials Modeling: Methods*; Yip, S., Ed.; Springer Netherlands: Dordrecht, 2005; pp 149–194.
(55) Zhu, B.; Meng, J.; Gao, Y. Equilibrium Shape of Metal Nanoparticles under Reactive Gas Conditions. *J. Phys. Chem. C* **2017**, *121*, 5629–5634.
(56) Zhao, P.; Cao, Z.; Liu, X.; Ren, P.; Cao, D.-B.; Xiang, H.; Jiao, H.; Yang, Y.; Li, Y.-W.; Wen, X.-D. Morphology and Reactivity Evolution of HCP and FCC Ru Nanoparticles under Co Atmosphere. *ACS Catal.* **2019**, *9*, 2768–2776.
(57) Li, W.-X.; Stampfl, C.; Scheffler, M. Why Is a Noble Metal Catalytically Active? The Role of the O-Ag Interaction in the Function of Silver as an Oxidation Catalyst. *Phys. Rev. Lett.* **2003**, *90*, 256102.
(58) Mittendorfer, F.; Seriani, N.; Dubay, O.; Kresse, G. Morphology of Mesoscopic Rh and Pd Nanoparticles under Oxidizing Conditions. *Phys. Rev. B: Condens. Matter Mater. Phys.* **2007**, *76*, 233413.
(59) Wulff, G. Xxv. Zur Frage Der Geschwindigkeit Des Wachsthums Und Der Auflösung Der Krystallflächen. *Z. Kristallogr. - Cryst. Mater.* **1901**, *34*, 449–530.
(60) Momma, K.; Izumi, F. Vesta 3 for Three-Dimensional Visualization of Crystal, Volumetric and Morphology Data. *J. Appl. Crystallogr.* **2011**, *44*, 1272–1276.

https://dx.doi.org/10.1021/acs.jpcc.0c07386
J. Phys. Chem. C XXXX, XXX, XXX–XXX

(61) Patanou, E.; Tveten, E. Z.; Chen, D.; Holmen, A.; Blekkan, E. A. Microcalorimetric Studies of H_2 and Co on Co//-Al_2O_3 Catalysts for Fischer−Tropsch Synthesis. *Catal. Today* **2013**, *214*, 19−24.
(62) Stroppa, A.; Kresse, G. The Shortcomings of Semi-Local and Hybrid Functionals: What We Can Learn from Surface Science Studies. *New J. Phys.* **2008**, *10*, 063020.
(63) Schimka, L.; Harl, J.; Stroppa, A.; Grüneis, A.; Marsman, M.; Mittendorfer, F.; Kresse, G. Accurate Surface and Adsorption Energies from Many-Body Perturbation Theory. *Nat. Mater.* **2010**, *9*, 741−744.
(64) Ge, Q.; Neurock, M. Adsorption and Activation of Co over Flat and Stepped Co Surfaces: A First Principles Analysis. *J. Phys. Chem. B* **2006**, *110*, 15368−15380.
(65) Zijlstra, B.; Broos, R. J. P.; Chen, W.; Oosterbeek, H.; Filot, I. A. W.; Hensen, E. J. M. Coverage Effects in Co Dissociation on Metallic Cobalt Nanoparticles. *ACS Catal.* **2019**, *9*, 7365−7372.
(66) Bridge, M. E.; Comrie, C. M.; Lambert, R. M. Chemisorption Studies on Cobalt Single Crystal Surfaces: I. Carbon Monoxide on Co(0001). *Surf. Sci.* **1977**, *67*, 393−404.
(67) Papp, H. The Chemisorption of Carbon Monoxide on a Co(0001) Single Crystal Surface; Studied by Leed, Ups, Eels, Aes and Work Function Measurements. *Surf. Sci.* **1983**, *129*, 205−218.
(68) Pfnür, H.; Menzel, D.; Hoffmann, F. M.; Ortega, A.; Bradshaw, A. M. High Resolution Vibrational Spectroscopy of Co on Ru(001): The Importance of Lateral Interactions. *Surf. Sci.* **1980**, *93*, 431−452.
(69) Weststrate, C. J.; van de Loosdrecht, J.; Niemantsverdriet, J. W. Spectroscopic Insights into Cobalt-Catalyzed Fischer−Tropsch Synthesis: A Review of the Carbon Monoxide Interaction with Single Crystalline Surfaces of Cobalt. *J. Catal.* **2016**, *342*, 1−16.
(70) Gunasooriya, G. T. K. K.; Saeys, M. Co Adsorption on Pt(111): From Isolated Molecules to Ordered High-Coverage Structures. *ACS Catal.* **2018**, *8*, 10225−10233.
(71) Biberrian, J. P.; Van Hove, M. A. A New Model for Co Ordering at High Coverages on Low Index Metal Surfaces: A Correlation between Leed, Hreels and Irs: Ii. Co Adsorbed on FCC (111) and HCP (0001) Surfaces. *Surf. Sci.* **1984**, *138*, 361−389.
(72) Steininger, H.; Lehwald, S.; Ibach, H. On the Adsorption of Co on Pt(111). *Surf. Sci.* **1982**, *123*, 264−282.
(73) Persson, B. N. J.; Tüshaus, M.; Bradshaw, A. M. On the Nature of Dense Co Adlayers. *J. Chem. Phys.* **1990**, *92*, 5034−5046.
(74) Avery, N. R. Electron Energy Loss Spectroscopic Study of Co on Pt(111). *J. Chem. Phys.* **1981**, *74*, 4202−4203.
(75) Bealing, C. R.; Baumgardner, W. J.; Choi, J. J.; Hanrath, T.; Hennig, R. G. Predicting Nanocrystal Shape through Consideration of Surface-Ligand Interactions. *ACS Nano* **2012**, *6*, 2118−2127.
(76) Nguyen, V. B.; Benoit, M.; Combe, N.; Tang, H. Prediction of Co Nanoparticle Morphologies Stabilized by Ligands: Towards a Kinetic Model. *Phys. Chem. Chem. Phys.* **2017**, *19*, 4636−4647.
(77) Lu, Y.; Zhang, H.; Wu, F.; Liu, H.; Fang, J. Size-Tunable Uniform Gold Octahedra: Fast Synthesis, Characterization, and Plasmonic Properties. *RSC Adv.* **2017**, *7*, 18601−18608.
(78) Zhang, J.; Gao, Y.; Alvarez-Puebla, R. A.; Buriak, J. M.; Fenniri, H. Synthesis and SERS Properties of Nanocrystalline Gold Octahedra Generated from Thermal Decomposition of $HAuCl_4$ in Block Copolymers. *Adv. Mater.* **2006**, *18*, 3233−3237.
(79) Zhang, J.; Liu, H.; Wang, Z.; Ming, N. Synthesis of Gold Regular Octahedra with Controlled Size and Plasmon Resonance. *Appl. Phys. Lett.* **2007**, *90*, 163122.
(80) Li, C.; Shuford, K. L.; Park, Q. H.; Cai, W.; Li, Y.; Lee, E. J.; Cho, S. O. High-Yield Synthesis of Single-Crystalline Gold Nano-Octahedra. *Angew. Chem., Int. Ed.* **2007**, *46*, 3264−3268.
(81) Wang, Y.; Wan, D.; Xie, S.; Xia, X.; Huang, C. Z.; Xia, Y. Synthesis of Silver Octahedra with Controlled Sizes and Optical Properties Via Seed-Mediated Growth. *ACS Nano* **2013**, *7*, 4586−4594.
(82) Wang, X.; Yuan, F.; Hu, P.; Yu, L.; Bai, L. Self-Assembled Growth of Hollow Spheres with Octahedron-Like Co Nanocrystals Via One-Pot Solution Fabrication. *J. Phys. Chem. C* **2008**, *112*, 8773−8778.
(83) Yu, M.; Liu, L.; Jia, L.; Li, D.; Wang, Q.; Hou, B. Equilibrium Morphology Evolution of FCC Cobalt Nanoparticle under Co and Hydrogen Environments. *Appl. Surf. Sci.* **2020**, *504*, 144469.
(84) Xiong, Y.; Washio, I.; Chen, J.; Cai, H.; Li, Z.-Y.; Xia, Y. Poly(Vinyl Pyrrolidone): A Dual Functional Reductant and Stabilizer for the Facile Synthesis of Noble Metal Nanoplates in Aqueous Solutions. *Langmuir* **2006**, *22*, 8563−8570.
(85) Zhou, S.; Wen, M.; Wang, N.; Wu, Q.; Wu, Q.; Cheng, L. Highly Active NiCo Alloy Hexagonal Nanoplates with Crystal Plane Selective Dehydrogenation and Visible-Light Photocatalysis. *J. Mater. Chem.* **2012**, *22*, 16858−16864.

https://dx.doi.org/10.1021/acs.jpcc.0c07386
J. Phys. Chem. C XXXX, XXX, XXX−XXX